Fe(001) angle-resolved photoemission and intrinsic anomalous Hall conductivity in Fe seen by different *ab initio* approaches: LDA and GGA versus *GW*

E. Młyńczak,[1,2,*] I. Aguilera,[1,†] P. Gospodarič,[1] T. Heider,[1] M. Jugovac,[1,‡] G. Zamborlini,[1,§] J.-P. Hanke,[1,3] C. Friedrich,[1] Y. Mokrousov,[1,3] C. Tusche,[1,4] S. Suga,[1,5] V. Feyer,[1] S. Blügel,[1] L. Plucinski,[1] and C. M. Schneider[1,4]

[1]*Peter Grünberg Institut PGI, Forschungszentrum Jülich and JARA- Fundamentals of Future Information Technologies, 52425 Jülich, Germany*

[2]*Jerzy Haber Institute of Catalysis and Surface Chemistry, Polish Academy of Sciences, Niezapominajek 8, 30-239 Krakow, Poland*

[3]*Institute of Physics, Johannes Gutenberg University Mainz, 55099 Mainz, Germany*

[4]*Fakultät für Physik, Universität Duisburg-Essen, 47057 Duisburg, Germany*

[5]*SANKEN, Osaka University, Ibaraki, Osaka 567-0047, Japan*

(Received 7 December 2021; revised 28 February 2022; accepted 21 March 2022; published 28 March 2022)

Many material properties such as the electronic transport characteristics depend on the details of the electronic band structure in the vicinity of the Fermi level. For an accurate *ab initio* description of the material properties, the electronic band structure must be known and theoretically reproduced with high fidelity. Here, we ask a question which of the *ab initio* methods compare the best to the experimental photoemission intensities from bcc Fe. We confront the photoemission data from Fe(001) thin film grown on Au(001) to the photoemission simulations based on different *ab initio* initial band structures: density functional theory (DFT) in the local density approximation (LDA) and the generalized gradient approximation (GGA) and GGA corrected with many-body perturbation theory in the *GW* approximation. We find the best comparison for the *GW* results. As a second step, we discuss how the calculated intrinsic anomalous Hall conductivity (AHC) in bcc Fe depends on the choice of the method that describes the electronic band structure and Fermi level position. We find very large differences in AHC between the three theoretical approaches and show that the AHC found for the experimental Fermi level location within the *GW* band structure is the closest to the literature results of transport experiments. This finding improves our understanding of not only the anomalous Hall effect itself, but also other related phenomena, such as the anomalous Nernst effect.

DOI: 10.1103/PhysRevB.105.115135

I. INTRODUCTION

In electronic band structures studies, the experiment and theory go hand in hand. Experimental electronic dispersions and shapes of Fermi surfaces can be used to draw conclusions on the material properties ranging from electric conductivity [1] to nontrivial topologies [2]. However, to thoroughly understand the underlying physics that allows meaningful predictions of the material properties, *ab initio* calculations are indispensable. Preferably, the electronic band structure that the theory reproduces must be as close as possible to the real electronic band structure of a material of interest, including the correct location of the Fermi level. This is, however, often difficult to ascertain as not always a direct correspondence between the experimental result and theory exists.

The *k*-resolved photoemission spectroscopy is an experimental method that enables precise determination of the electronic dispersions in momentum space. However, a photoemission result does not directly correspond to the ground state electronic structure, because of the several reasons. First, the photoemission transition probability involves interband selection rules and matrix elements. As a consequence, a photoemission experiment will only see those bands compatible with the selection rules for the chosen experimental geometry. Second, because each photoexcited electron leaves a hole behind, only the excited state that contains (N-1) electrons (where N is the total number of electrons in the sample) can be addressed experimentally. In this context, one speaks of the so-called quasiparticle band structure, where quasiparticles (quasiholes and quasielectrons) can be regarded as (superpositions of) true many-body states.

Within Kohn-Sham density-functional theory (DFT) [3,4], the interacting many-electron system is mapped onto a non-interacting system of electrons, the so-called Kohn-Sham system, whose time-independent Schrödinger equation can be solved straightforwardly. The Kohn-Sham system is constructed such that a self-consistent solution yields an approximate ground-state electronic density of the interacting system and, derived from it, other ground-state properties such as the ground-state total energy, atomic forces, etc. The results depend on the approximation for the exchange-correlation energy functional used in the DFT calculation. The most common variants are the local-density approximation (LDA),

*ewa.mlynczak@ikifp.edu.pl

†Current address: Institute of Physics, University of Amsterdam, Netherlands.

‡Current address: Elettra - Sincrotrone Trieste, S.S. 14 km 163.5 in AREA Science Park, Basovizza, I-34149 Trieste, Italy.

§Current address: Technische Universität Dortmund, Experimentelle Physik VI, 44227 Dortmund, Germany.

which approximates the exchange-correlation energy density locally by the one of the homogeneous electron gas with the same (local) electronic density, and the generalized gradient approximation (GGA), in which the gradient of the electronic density is taken into account in addition. Even though DFT is thus made for describing the electronic ground state, it is broadly used to interpret the band structures of real materials measured in photoemission experiments [5,6]. However, there is no theoretical justification for this interpretation [7]. What is more, based on a comparison between DFT band structure and the photoemission results, one often discusses correlation effects, which cause, e.g., bandwidth and electron mass renormalization [5]. For Fe(110) the bandwidth reduction of 30% was obtained by the comparison of the photoemission result with the GGA band structure [5], which suggest that Fe is a strongly correlated material, similarly to Ni. In the same paper, very strong electron mass renormalizations reaching a factor of 3 were reported [5]. Later, it was pointed out by Walter *et al.* [6], that already including the final state effects *via* broadening along the wave vector perpendicular to the sample surface results in more modest renormalization values as compared to the estimates based on theoretical band structures [5]. Moreover, the unsatisfactory comparison of the spin-resolved photoemission intensities from Fe(110) with the results of calculations performed using dynamical mean-field theory and three-body scattering approximation combined with one-step model calculations of the photoemission called for the necessity to include nonlocal effects in the theoretical description of the electronic band structure of Fe [8,9]. The pronounced contribution of the nonlocal correlations was previously demonstrated for Co [10].

An alternative way to calculate quasiparticle band structures is many-body perturbation theory, whose basic quantity is the one-particle Green function. In principle, the Green function encodes all excited states of the (N-1) [and (N+1)] electron system, precisely those that are relevant for photoemission spectroscopy. Practical calculations rely on an approximation for the electronic self-energy. The simplest one beyond the Hartree-Fock approximation is the *GW* self-energy [11], where G and W stand for the Green function and dynamically screened interaction, respectively. The *GW* self-energy is nonlocal and energy (or time) dependent.

In the last decades, the *GW* method has been very successful, especially in the correct predictions of the band gaps with respect to LDA [8], but it is also known to improve the description of the band structure of metals [12] when compared to experimental photoemission data. However, still due to its computational demand and complexity, the *GW* method is not as commonly used as could be expected, and it is often replaced by simpler DFT approaches.

One of the phenomena that is known to critically depend on the characteristics of the electronic band structure is the intrinsic anomalous Hall effect (AHE), i.e., the occurrence of the transversal voltage V_{xy} when a longitudinal current flows through the ferromagnetic sample placed in the magnetic field (both magnetization and the external magnetic field are along the z direction). Whereas the *extrinsic* AHE depends on scattering on the impurities, the *intrinsic* AHE emerges directly from the properties of the band structure [13–15]. Following the original ideas of Karplus and Luttinger [16], the intrinsic AHE has been explained in the language of the Berry phase [17] and has been widely studied via the *ab initio* approach [18]. The intrinsic AHE effect is known to be very sensitive to the details of the electronic band structure near the Fermi level, especially to the presence of the spin-orbit gaps, which resonantly enhance the transversal conductivity (σ_{xy}) [13–15,19]. The intrinsic AHE occurs also in ferromagnetic Weyl metals, where it can be entirely associated with the Weyl nodes that are the monopole sources of the Berry curvature [20]. By decomposing contributions to the intrinsic AHE in bcc Fe into particular Fermi sheets, it was found that the large Fermi sheets that have chiral Weyl nodes nearby in momentum space contribute the most to the total anomalous Hall conductivity (AHC) [21]. Moreover, the small Fermi sheet pockets that were identified to be topologically nontrivial, also contributed a significant 20% of the total value of the AHC [21].

In this article we ask the question if and to what extent the use of *GW* improves the theoretical estimate of the bcc Fe band structure, as compared to LDA and GGA. We compare the experimentally measured photoemission intensities from Fe(001) with the theoretical electronic band structures. We do not only take into account the actual quasiparticle band structure but also perform photoemission simulations to account for the intrinsic broadening of the final state along the $k_\perp$ direction [22].

In a second step, we present calculations of the intrinsic anomalous Hall conductivity of bcc Fe based on LDA, GGA, and *GW* approximation. We show that the *GW* method is the most accurate in describing the electronic band structure of Fe and consequently its application leads to the best estimate for the intrinsic anomalous Hall effect, in particular when the experimental Fermi level is taken into account.

II. EXPERIMENTAL AND THEORETICAL METHODS

The 40-monolayer (ML) Fe films were grown *in situ* on Au(001) single crystal at low temperature (T = 100K) using molecular beam epitaxy and gently annealed up to 600 K. This preparation procedure was found previously to result in high quality Fe(001) films, with no Au present on Fe surface [24], which was confirmed in the present experiment by XPS measurements. Mapping of the electronic dispersions was performed using the momentum microscope at the NanoESCA beamline at the Elettra synchrotron in Trieste (Italy) [25]. These measurements were performed using photon energy of $h\nu = 70$ eV with different light polarizations: linear s- and circularly left- and right-polarized light (σ^- and σ^+) while keeping the sample at about the liquid nitrogen temperature (T = 90 K).

First-principles calculations were carried out within the all-electron full-potential linearized augmented-plane-wave (FLAPW) formalism with the FLEUR [26] and SPEX [27] codes. For the LDA and GGA calculations, we used an angular momentum cutoff of $l_{\max} = 8$ in the atomic spheres and a plane-wave cutoff of 5.0 bohr^{-1} in the interstitial region. For the lattice parameter we used a value of 2.87 Å. The $3s$ and $3p$ orbitals were treated as semicore by the use of local orbitals. The GGA result was then used as a starting point for the *GW* approach. The mixed product basis [27] used in the

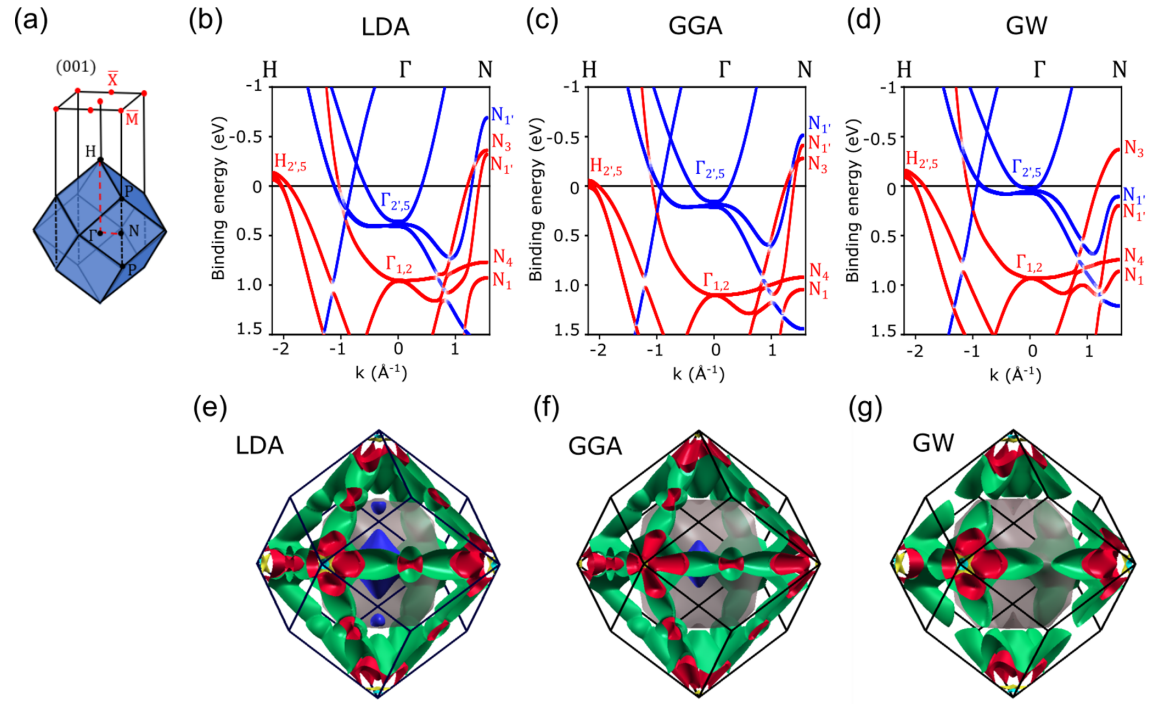

FIG. 1. (a) A sketch of the bulk Brillouin zone of bcc Fe and (001) surface Brillouin zone with an exemplary H-Γ-N path indicated by a red dashed line. [(b)–(d)] Bulk electronic band structures of bcc Fe along H-Γ-N line as given by LDA, GGA, and *GW* methods, including spin-orbit coupling. Blue and red color mark the states of predominantly minority and majority spin character. The high symmetry points are also indicated. [(e)–(g)] Three-dimensional visualization of Fermi surfaces given by LDA, GGA, and *GW* methods. The figures were prepared using XCRYSDEN software [23].

GW calculation was constructed with an angular momentum cutoff of $l_{\max} = 4$ and a plane-wave cutoff of 3.0 bohr^{-1}. We used 170 unoccupied bands and a 10×10×10 **k**-point sampling of the Brillouin zone. Two additional local orbitals per angular momentum up to $l = 3$ were included to describe high-lying states accurately and to avoid linearization errors [28]. However, for the photoemission simulation, a much denser mesh of 200×200×200 k points was used. We made use of the Wannier interpolation technique [29] to generate the data on the required k-point mesh. The Wannier functions were obtained with the WANNIER90 library [30].

In the photoemission simulation we assumed that the final electron state is a free electron. Then, the value of the perpendicular wave vector probed in the experiment for a given kinetic energy E_{kin} and emission angle Θ can be found as

$$k_{\perp}^{0} = \sqrt{(2m/\hbar^2)(E_{\text{kin}}\cos^2\theta + V_0)}, \tag{1}$$

where V_0 stands for the value of the inner potential, adjusted by comparison with the experiment to be equal to 11 eV, m is the electron mass taken here to be equal to the rest mass of the electron, i.e., 0.511 MeV/c^2. In addition, we integrate the initial electronic states around $k_{\perp}^{0}$ to account for the intrinsic broadening of the final state ($\Delta k_{\perp}$) [22,31,32]. The broadening of the final state along the perpendicular wave vector is related via the Heisenberg principle with the inelastic mean free path, understood as uncertainty of the final state electron location. We also assumed the matrix element as well as surface transmission to be equal to unity [22]. We included energy broadening equal to the experimental energy resolution, $\Delta E = 50$ meV. The simulations were performed using the same scheme as presented in Ref. [22]

Starting from the LDA, GGA, and *GW* electronic structures we again employed the Wannier interpolation [15,30,33], this time to efficiently evaluate the intrinsic anomalous Hall conductivity:

$$\sigma_{xy} = \frac{2e^2}{\hbar}\text{Im}\sum_{n}^{\text{occ}}\int \frac{dk^3}{(2\pi)^3}\left\langle \frac{\partial u_{kn}}{\partial k_x}\middle|\frac{\partial u_{kn}}{\partial k_y}\right\rangle, \tag{2}$$

where the summation is restricted to all occupied bands, k is the crystal momentum, $|u_{kn}\rangle$ is an eigenstate of the lattice-periodic Hamiltonian, and e is the elementary charge. Based on the Wannier interpolation, the Brillouin-zone integration was performed on an ultradense mesh of 512 × 512 × 512 k points.

III. EXPERIMENTAL AND THEORETICAL RESULTS

A. Bulk electronic band structure of bcc Fe

We begin with the presentation of the bulk electronic band structure of bcc Fe given by LDA, GGA and *GW* methods along the H−Γ−N line [Figs. 1(b)–1(d), bulk Brillouin zone of bcc Fe is sketched in Fig. 1(a)]. The respective Fermi surfaces are visualized in Figs. 1(e)–1(g). Comparing LDA and GGA band structures [Figs. 1(b) and 1(c)] one can see that GGA differs from the LDA result by significant shifts of the bands on the energy scale, in both directions (compare positions of the minority $\Gamma_{2',5}$ and the majority $\Gamma_{1,2}$ points). Differences in the energetic positions of the bands are of the order

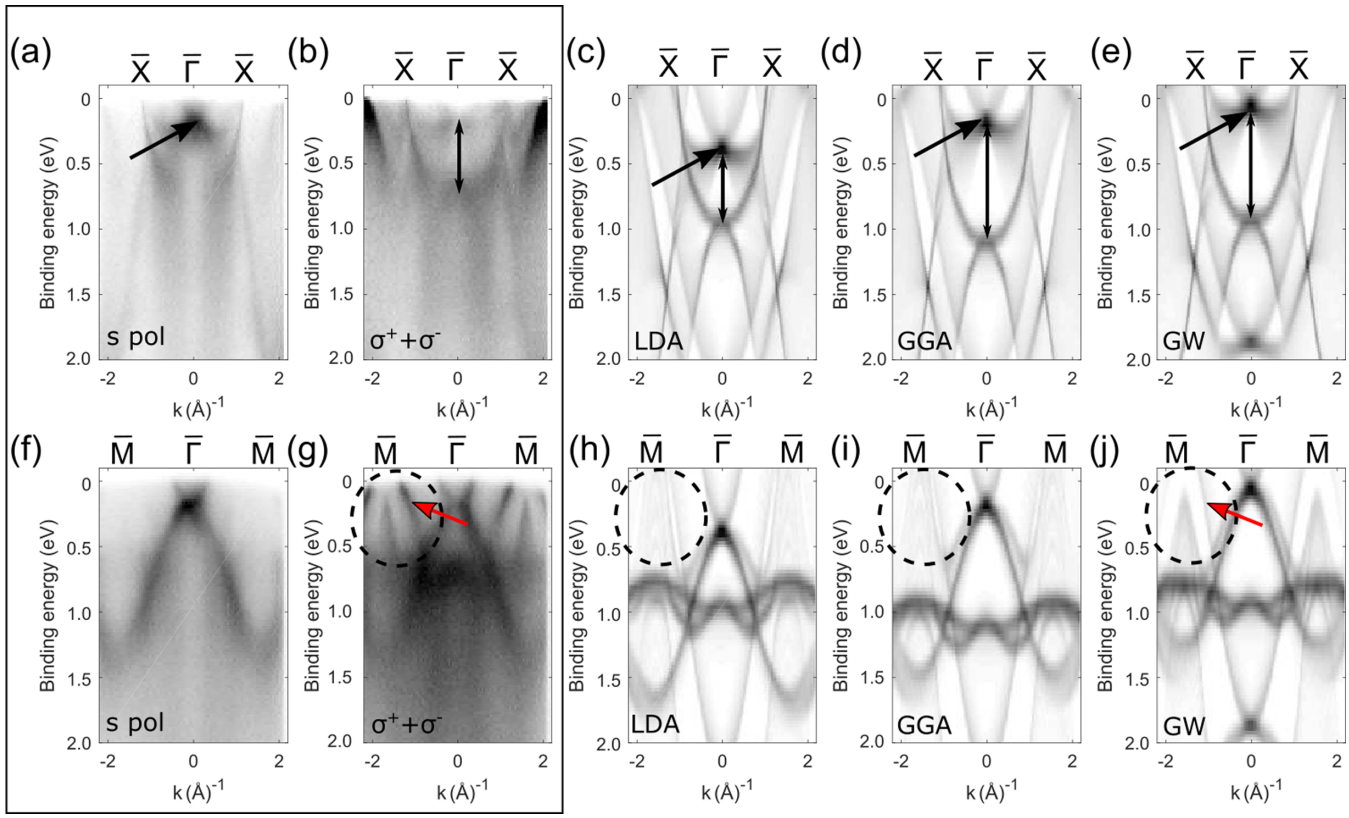

FIG. 2. [(a),(b)] The experimental dispersions along $\overline{\mathrm{X}}-\overline{\Gamma}-\overline{\mathrm{X}}$ direction measured on Fe(001). The result for s-polarized light as well as the sum of the results obtained using two circular polarizations $\sigma^+ + \sigma^-$ are shown in (a) and (b), respectively. [(c)–(e)] Results of the photoemission simulation along $\overline{\mathrm{X}}-\overline{\Gamma}-\overline{\mathrm{X}}$ when the initial electronic band structure is described by LDA, GGA, and *GW* methods, respectively. [(f)-(j)] Same as (a)–(e) for the $\overline{\mathrm{M}}-\overline{\Gamma}-\overline{\mathrm{M}}$ direction. Dashed circles indicate regions of interest discussed in the main text. Double-sided black arrows mark characteristic distances on the energy scale. A red arrow in (g) indicates experimental position of one of the characteristic hole bands at the $\overline{\mathrm{M}}$ point.

of 150 meV, reaching roughly 200 meV at the $\Gamma_{2',5}$ point. Especially interesting is the situation at the N point, where the three hole bands with maxima above the Fermi level switch order on the energy scale. Note that the majority spin N_1' point nearly touches the N_3 point in the LDA result [N_1' point is located 5 meV below the N_3 point, Fig. 1(b)], while being shifted significantly as high as 100 meV above the N_3 point in the GGA result [Fig. 1(c)]. When the *GW* approximation is invoked [Fig. 1(d)], most of the bands are shifted up on the energy scale, and the shifts are of the order of 150 meV with respect to the GGA result. Once more, the most interesting situation is encountered at the N point, where the majority spin N_3 point is moved significantly up, while the minority spin N_1' and majority spin N_1' points are pushed below the Fermi level. This has a serious consequence, as these bands do not contribute to the Fermi surface any more. This is visualized in Figs. 1(e)–1(g), where the circular Fermi sheet surrounding the N point is not present in the *GW* result [Fig. 1(g)].

B. Photoemission results from Fe(001)

We start from discussing the experimental dispersions measured along two principle directions within the surface Brillouin zone of Fe(001), i.e., $\overline{\mathrm{X}}-\overline{\Gamma}-\overline{\mathrm{X}}$ and $\overline{\mathrm{M}}-\overline{\Gamma}-\overline{\mathrm{M}}$, which correspond to in-plane [100] and [110] directions in real space, and contain the projection of the Γ-H and Γ-N directions, respectively [Figs. 2(a) and 2(b), and 2(f) and 2(g)]. The results obtained using s-polarized light are shown in Figs. 2(a) and 2(f), while Figs. 2(b) and 2(g) show the sum of the results obtained using left and right circular polarizations ($\sigma^+ + \sigma^-$). In order to compare the theoretical predictions with the experimental results, we performed photoemission simulations [22] based on the LDA, GGA, and *GW* initial band structures, which are shown in Figs. 2(c)–2(e) and 2(h)–2(j), respectively. The photoemission simulation method that we use does not include dipole selection rules, therefore all of the initial states that can potentially contribute to photoemission for a given light energy are visualized, irrespective of the orbital symmetry of the states. In the experiment we use a photon energy of $E_{h\nu}$ =70 eV, which results in the photoexcitation from a range of initial states with a wave vector spread of $\Delta k_\perp \sim 0.3$ Å^{-1} around the Γ point [22]. The experimentally observed states can be attributed to the bulk bands after consideration of the dipole transition matrix elements [34]. We note here, that we do not experimentally observe any states that could be attributed to surface electronic states of Fe(001), similarly to the results published in Ref. [22,24,34]. While the result obtained using s-polarized light represents only a subset of bulk bands, as dictated by the dipole selection rules [34], the "$\sigma^+ + \sigma^-$" results contain the electronic states of all orbital symmetries, which facilitates comparison to the photoemission simulation. Here, we will

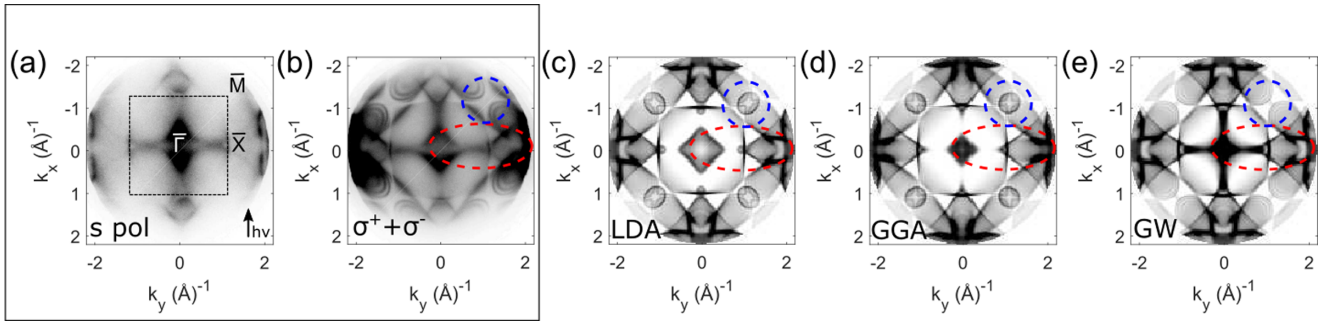

FIG. 3. [(a),(b)] The experimental constant energy cuts near the Fermi level ($E_b = 0.05$ eV) measured on Fe(001). The result for s-polarized light as well as the sum of the results obtained using two circular polarizations $\sigma^+ + \sigma^-$ are shown in (a) and (b), respectively. An arrow in (a) indicates photons incidence direction, which impinge at the angle of 25° with respect to the sample surface. [(c)–(e)] Results of the photoemission simulation when the initial electronic band structure is described by LDA, GGA, and *GW* methods, respectively. The dashed square in (a) marks the surface Brillouin zone, while the blue and red dashed ellipsoids in (b)–(e) encircle the regions of interest discussed in the text.

focus on the comparison of the experimental result to the three theoretical predictions. In the experimental result along $\overline{\mathrm{X}} - \overline{\Gamma} - \overline{\mathrm{X}}$ line, we observe a characteristic region of high spectral intensity located at the Γ point at $E_b = 0.175$ eV [marked by an arrow in Fig. 2(a), which contains a bulk $\Gamma_{2',5}$ point where the minority Δ_2' and Δ_5 bands meet, see Ref. [34] for the complete identification of the experimental features along $\overline{\mathrm{X}} - \overline{\Gamma} - \overline{\mathrm{X}}$ line]. This feature can be easily identified in the photoemission simulations [Figs. 2(c)–2(e)], and in accord with the result of the shifts of $\Gamma_{2',5}$ point in the bulk (Fig. 1), its position on the energy scale is largely different in the three cases. Clearly, LDA predicts it to be located far too deep [$E_b = 0.4$ eV, Fig. 2(c)], but already GGA corrects its position to $E_b = 0.2$ eV, while *GW* result predicts it position to be slightly too close to the Fermi level $E_b = 0.05$ eV.

In addition, we can also compare an absolute energy distance between the two characteristic points at the $\overline{\Gamma}$ point: the point of high spectral intensity mentioned above and the bottom of the parabolic Δ_1 band [34]. This distance, equal in the experiment to roughly 0.5 eV, is marked by a double-sided arrow in Figs. 2(b)–2(e). The LDA result provides a value very close to the experiment, while both GGA and *GW* predictions overestimate it significantly (0.95 eV and 0.9 eV, respectively). This observation suggests that the LDA prediction could become very similar to the experimental result when only a Fermi level position had been shifted. Why this is actually *not* the case, we can learn from the analysis of the dispersions along the $\overline{\mathrm{M}} - \overline{\Gamma} - \overline{\mathrm{M}}$ line [Figs. 2(f)–2(j)]. Along this direction we can clearly see the electronic bands at the $\overline{\mathrm{M}}$ point, which directly correspond to the bulk bands located at the *N* point, which were shown in Fig. 1 and discussed above. The experimental result [Fig. 2(g)] is clear: The two hole bands at the $\overline{\mathrm{M}}$ point (that correspond to the minority and majority spin bulk bands labeled by high-symmetry points $\mathrm{N}_{1'}$ in Fig. 1) barely touch the experimental Fermi level (visible within the dashed circle), while the flatter top one (that correspond to the majority spin band labeled by a high-symmetry point N_3 in Fig. 1) is significantly shifted up in energy [marked by a red arrow in Fig. 2(g)]. These very bands are shifted too much up in the LDA result [Fig. 2(h), region within the dashed circle]. If the Fermi level would be shifted in the LDA result to match the experimental bands along the $\overline{\mathrm{X}} - \overline{\Gamma} - \overline{\mathrm{X}}$ direction [Figs. 2(a)–2(c)], the comparison to the experiment at the $\overline{\mathrm{M}}$ point would become even worse. On the other hand, the *GW* result reproduces the situation at the $\overline{\mathrm{M}}$ point with high fidelity, including the correct order of the bands. The two hole bulk bands at the $\overline{\mathrm{M}}$ point labeled by $\mathrm{N}_{1'}$ high-symmetry labels in Fig. 1 are not distinguished in the experiment, which is in agreement with the *GW* photoemission simulation [Fig. 2(j)].

In the following, we will present the experimental constant energy cuts near the Fermi level [Fig. 3(a) and 3(b), the measurement performed using s-polarized light and the sum of two circular polarizations, left and right, respectively]. In Fig. 3(a), the surface Brillouin zone (SBZ) is marked by a dotted square. We identify two characteristic regions: one along the $\overline{\mathrm{X}} - \overline{\Gamma} - \overline{\mathrm{X}}$ line, which corresponds to the projection along $\Gamma-$ H line in the BBZ (marked by a red-dashed ellipse in Fig. 3), and the vicinity of the $\overline{\mathrm{M}}$ point, which results from the projection along the line that contains the N point from the bulk Brillouin zone (BBZ) (marked by a blue circle in Fig. 3). In the area within the red ellipse, the experiment shows a continuous shape that connects the central Fermi sheet to the one in the vicinity of the $\overline{\mathrm{X}}$ point [Fig. 3(b)], which is correctly reproduced only by the *GW* result [Fig. 3(e)]. Around the $\overline{\mathrm{M}}$ point (the blue circle), the experiment reveals the absence of the circular Fermi sheet predicted by LDA and GGA methods [Figs. 3(b)–3(d)], again being in accordance with the *GW* prediction [Fig. 3(e)].

We conclude, that even though the energetic distance between the features at the $\overline{\Gamma}$ point is overestimated by the *GW* method [Figs. 2(g) and 2(j)], the position and order of the bands close to the Fermi level matches the experiment the best, in comparison to the simulations based on LDA and GGA initial band structures.

C. Intrinsic anomalous Hall effect in bcc Fe

Even though the intrinsic AHE depends purely on the properties of the electronic band structure, there exists a significant discrepancy between the typically calculated values of the AHC in bcc Fe, which are equal to approximately 750–770 S/cm when the GGA band structures are assumed [14,15,35], and the experimental results, which give values

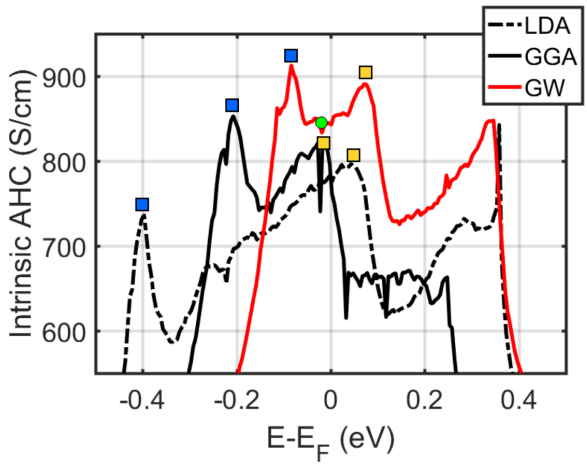

FIG. 4. First-principles results for the intrinsic anomalous Hall conductivity of bcc Fe as a function of the position of the Fermi level, starting from the electronic structure calculated using LDA, GGA, and *GW* methods. The experimentally found position of the Fermi level ($E_F = 0.045$ eV below the theoretical *GW* Fermi level) is marked with a green dot. Blue and orange markers indicate characteristic maxima discussed in the text.

of $\sigma_{xy} \approx 1000$ S/cm [36–38]. This discrepancy might be attributed to the experimental uncertainties as well as to shortcomings of the GGA method in describing realistic electronic band structure of bcc Fe. It was previously found that the theoretical intrinsic contribution to AHC in Fe might reach the value of 827 S/cm but only after including an arbitrary shift of the band structure via a U parameter within the GGA+U approach [35].

To check the impact of the underlying theoretical description of the electronic structure on predictions of the intrinsic AHE, we have performed *ab initio* calculations of the intrinsic AHE in bcc Fe based on all three electronic band structures given by LDA, GGA, and *GW* methods.

The values of the transversal conductivity (σ_{xy}) were determined for different positions of the Fermi level (E_F), shifted with respect to the Fermi levels found in the respective theoretical methods (Fig. 4). It is evident that σ_{xy} shows a strong dependence on the underlying *ab initio* method. Furthermore, we see that a shift of the Fermi energy of only 100 meV can give rise to changes in the Hall conductivity of the order of 100 S/cm.

One can attempt to relate the peaks of the AHC to the specific points in the electronic band structure, even though the total AHC is a result of the summation over the entire Brillouin zone. For example, the two peaks closest to the *GW* E_F are marked by blue and orange markers in Fig. 4. The orange one coincides in the energetic position with the $H_{2'5}$ point (compare Fig. 1), which is known to be a hotspot of the Berry curvature when one of the spin-split branches lies above, and the other—below the Fermi level [15]. The blue one, that marks the maximum at $E_b = 0.085$ eV in the *GW* result coincides with the energetic position of the $\Gamma_{1,2}$ point. The corresponding maxima of AHC can be identified in the LDA and GGA results (Fig. 4), and are also marked with orange and blue markers. Their positions shift *in unisono* with the shifts of the $H_{2'5}$ and $\Gamma_{1,2}$ points in LDA and GGA band structures (Fig. 1). It becomes clear how important it is to accurately define the position of E_F within the correct initial electronic band structure to be able to faithfully estimate intrinsic AHC.

Using high-resolution angle-resolved photoemission, we have determined previously, that the experimental position of the Fermi level lies at $E_F = 0.045$ eV below the theoretical *GW* Fermi level [22]. Using this value for the E_F position, we obtain a transversal conductivity of $\sigma_{xy} = 845$ S/cm, which is much closer to the experimentally measured value of $\sigma_{xy} \approx 1000$ S/cm [36–38] than previously available results based on GGA band structures [14,15,35]. This result was obtained for the electronic band structure described fully *ab initio* (i.e., without the need of any adjustable parameter). If we regard it as an upper limit for the intrinsic contribution to AHC in bcc Fe, the remaining difference between the calculated and the experimentally obtained values should be ascribed to other ingredients of the AHC such as the side jump contribution [35] or the experimental uncertainties. This finding has important implications not only for the accurate comparison of the theoretical and experimental AHC but also for the understanding of other phenomena related to AHE such as the anomalous Nernst effect (ANE). The ANE depends on the values of the anomalous Hall conductivity below and above E_F and would vanish if the values of AHC would be a symmetric function around the Fermi level [39]. We finally note that the scattering on the impurities, which is a mechanism of the extrinsic contribution to AHC, also depends on the electronic band structure of the host material and the position of the Fermi level [40].

IV. SUMMARY AND CONCLUSIONS

In this paper, we have compared the theoretical *ab initio* band structures of bcc Fe as given by LDA, GGA, and *GW* approaches to the experimental electronic band structures measured for Fe(001). To achieve a meaningful comparison between the bulk *ab initio* result and the experimental photoemission result, we have employed photoemission simulations that take into account intrinsic broadening of the final state along the wave vector perpendicular to the sample surface. We have found that the best comparison between the experiment and the theory is obtained when the initial band structure is described using the *GW* method. To exemplify the possible implications of using different *ab initio* band structures to predict material properties we discuss the calculations of the intrinsic anomalous Hall effect. We find that using *GW* band structure to determine the intrinsic anomalous Hall conductivity results in the best agreement with the available transport data. This study elucidates the importance of an accurate description of the electronic structure for the interpretation of transport data. The *GW* approach may also improve the predictions of other fundamental properties of Fe including magnetic anisotropy and nontrivial topology.

ACKNOWLEDGMENTS

This work was supported by the Helmholtz Association via The Initiative and Networking Fund, by Alexander von Humboldt Foundation and by the statutory research funds of ICSC PAS within the subsidy of the Ministry of Education

and Science, Poland. The fruitful discussions with B. Zimmermann are acknowledged. We gratefully acknowledge the computing time granted through JARA-HPC on the supercomputer JURECA at Forschungszentrum Jülich.

[1] H.-J. Noh, J. Jeong, J. Jeong, E.-J. Cho, S. B. Kim, K. Kim, B. I. Min, and H.-D. Kim, Anisotropic Electric Conductivity of Delafossite $PdCoO_2$ Studied by Angle-Resolved Photoemission Spectroscopy, Phys. Rev. Lett. **102**, 256404 (2009).

[2] I. Belopolski, K. Manna, D. S. Sanchez, G. Chang, B. Ernst, J. Yin, S. S. Zhang, T. Cochran, N. Shumiya, H. Zheng *et al.*, Discovery of topological Weyl fermion lines and drumhead surface states in a room temperature magnet, Science **365**, 1278 (2019).

[3] P. Hohenberg and W. Kohn, Inhomogeneous electron gas, Phys. Rev. **136**, B864 (1964).

[4] W. Kohn and L. J. Sham, Self-consistent equations including exchange and correlation effects, Phys. Rev. **140**, A1133 (1965).

[5] J. Schäfer, M. Hoinkis, E. Rotenberg, P. Blaha, and R. Claessen, Fermi surface and electron correlation effects of ferromagnetic iron, Phys. Rev. B **72**, 155115 (2005).

[6] A. L. Walter, J. D. Riley, and O. Rader, Theoretical limitations to the determination of bandwidth and electron mass renormalization: the case of ferromagnetic iron, New J. Phys. **12**, 013007 (2010).

[7] F. Aryasetiawan and O. Gunnarsson, The *GW* method, Rep. Prog. Phys. **61**, 237 (1998).

[8] J. Sánchez-Barriga, J. Fink, V. Boni, I. Di Marco, J. Braun, J. Minár, A. Varykhalov, O. Rader, V. Bellini, F. Manghi, H. Ebert, M. I. Katsnelson, A. I. Lichtenstein, O. Eriksson, W. Eberhardt, and H. A. Dürr, Strength of Correlation Effects in the Electronic Structure of Iron, Phys. Rev. Lett. **103**, 267203 (2009).

[9] J. Sánchez-Barriga, J. Braun, J. Minár, I. Di Marco, A. Varykhalov, O. Rader, V. Boni, V. Bellini, F. Manghi, H. Ebert, M. I. Katsnelson, A. I. Lichtenstein, O. Eriksson, W. Eberhardt, H. A. Dürr, and J. Fink, Effects of spin-dependent quasiparticle renormalization in Fe, Co, and Ni photoemission spectra: An experimental and theoretical study, Phys. Rev. B **85**, 205109 (2012).

[10] C. Tusche, M. Ellguth, A. Krasyuk, C. Wiemann, J. Henk, C. M. Schneider, and J. Kirschner, Nonlocal electron correlations in an itinerant ferromagnet, Nat. Commun. **9**, 3727 (2018).

[11] L. Hedin, New method for calculating the one-particle green's function with application to the electron-Gas problem, Phys. Rev. **139**, A796 (1965).

[12] J. E. Northrup, M. S. Hybertsen, and S. G. Louie, Quasiparticle excitation spectrum for nearly-free-electron metals, Phys. Rev. B **39**, 8198 (1989).

[13] S. Onoda, N. Sugimoto, and N. Nagaosa, Intrinsic Versus Extrinsic Anomalous Hall Effect in Ferromagnets, Phys. Rev. Lett. **97**, 126602 (2006).

[14] Y. Yao, L. Kleinman, A. H. MacDonald, J. Sinova, T. Jungwirth, D. Sheng Wang, E. Wang, and Q. Niu, First Principles Calculation of Anomalous Hall Conductivity in Ferromagnetic bcc Fe, Phys. Rev. Lett. **92**, 037204 (2004).

[15] X. Wang, J. R. Yates, I. Souza, and D. Vanderbilt, *Ab initio* calculation of the anomalous Hall conductivity by Wannier interpolation, Phys. Rev. B **74**, 195118 (2006).

[16] R. Karplus and J. M. Luttinger, Hall effect in ferromagnetics, Phys. Rev. **95**, 1154 (1954).

[17] T. Jungwirth, Q. Niu, and A. H. MacDonald, Anomalous Hall Effect in Ferromagnetic Semiconductors, Phys. Rev. Lett. **88**, 207208 (2002).

[18] N. Nagaosa, J. Sinova, S. Onoda, A. H. MacDonald, and N. P. Ong, Anomalous Hall effect, Rev. Mod. Phys. **82**, 1539 (2010).

[19] Z. Fang, N. Nagaosa, K. S. Takahashi, A. Asamitsu, R. Mathieu, T. Ogasawara, H. Yamada, M. Kawasaki, Y. Tokura, and K. Terakura, The anomalous Hall effect and magnetic monopoles in momentum space, Science **302**, 92 (2003).

[20] A. A. Burkov, Anomalous Hall Effect in Weyl Metals, Phys. Rev. Lett. **113**, 187202 (2014).

[21] D. Gosálbez-Martínez, I. Souza, and D. Vanderbilt, Chiral degeneracies and Fermi-surface Chern numbers in bcc Fe, Phys. Rev. B **92**, 085138 (2015).

[22] E. Młyńczak, I. Aguilera, P. Gospodarič, T. Heider, M. Jugovac, G. Zamborlini, C. Tusche, S. Suga, V. Feyer, S. Blügel, L. Plucinski, and C. M. Schneider, Spin-polarized quantized electronic structure of Fe(001) with symmetry breaking due to the magnetization direction, Phys. Rev. B **103**, 035134 (2021).

[23] A. Kokalj, Computer graphics and graphical user interfaces as tools in simulations of matter at the atomic scale, Comput. Mater. Sci. **28**, 155 (2003).

[24] E. Młyńczak, M. Eschbach, S. Borek, J. Minár, J. Braun, I. Aguilera, G. Bihlmayer, S. Döring, M. Gehlmann, P. Gospodarič, S. Suga, L. Plucinski, S. Blügel, H. Ebert, and C. M. Schneider, Fermi Surface Manipulation by External Magnetic Field Demonstrated for a Prototypical Ferromagnet, Phys. Rev. X **6**, 041048 (2016).

[25] C. Tusche, A. Krasyuk, and J. Kirschner, Spin resolved bandstructure imaging with a high resolution momentum microscope, Ultramicroscopy **159**, 520 (2015).

[26] http://www.flapw.de.

[27] C. Friedrich, S. Blügel, and A. Schindlmayr, Efficient implementation of the *GW* approximation within the all-electron FLAPW method, Phys. Rev. B **81**, 125102 (2010).

[28] C. Friedrich, A. Schindlmayr, S. Blügel, and T. Kotani, Elimination of the linearization error in GW calculations based on the linearized augmented-plane-wave method, Phys. Rev. B **74**, 045104 (2006).

[29] N. Marzari, A. A. Mostofi, J. R. Yates, I. Souza, and D. Vanderbilt, Maximally localized Wannier functions: Theory and applications, Rev. Mod. Phys. **84**, 1419 (2012).

[30] A. A. Mostofi, J. R. Yates, G. Pizzi, Y. S. Lee, I. Souza, D. Vanderbilt, and N. Marzari, An updated version of wannier90: A tool for obtaining maximally-localised Wannier functions, Comput. Phys. Commun. **185**, 2309 (2014).

[31] R. Matzdorf, UV-photoelectron spectroscopy at highest resolution—Direct access to lifetime effects in solids? Appl. Phys. A **63**, 549 (1996).

[32] V. Strocov, Intrinsic accuracy in 3-dimensional photoemission band mapping, J. Electron Spectrosc. Relat. Phenom. **130**, 65 (2003).

[33] J. R. Yates, X. Wang, D. Vanderbilt, and I. Souza, Spectral and Fermi surface properties from Wannier interpolation, Phys. Rev. B **75**, 195121 (2007).

[34] E. Młyńczak, M. C. T. D. Müller, P. Gospodarič, T. Heider, I. Aguilera, M. Gehlmann, M. Jugovac, G. Zamborlini, C. Tusche, S. Suga, V. Feyer, L. Plucinski, C. Friedrich, S. Blügel, and C. M. Schneider, Kink far below the Fermi level reveals new electron-magnon scattering channel in Fe, Nat. Commun. **10**, 505 (2019).

[35] J. Weischenberg, F. Freimuth, J. Sinova, S. Blügel, and Y. Mokrousov, *Ab Initio* Theory of the Scattering-Independent Anomalous Hall Effect, Phys. Rev. Lett. **107**, 106601 (2011).

[36] T. Miyasato, N. Abe, T. Fujii, A. Asamitsu, S. Onoda, Y. Onose, N. Nagaosa, and Y. Tokura, Crossover Behavior of the Anomalous Hall Effect and Anomalous Nernst Effect in Itinerant Ferromagnets, Phys. Rev. Lett. **99**, 086602 (2007).

[37] Y. Tian, L. Ye, and X. Jin, Proper Scaling of the Anomalous Hall Effect, Phys. Rev. Lett. **103**, 087206 (2009).

[38] S. Sangiao, L. Morellon, G. Simon, J. M. De Teresa, J. A. Pardo, J. Arbiol, and M. R. Ibarra, Anomalous Hall effect in Fe (001) epitaxial thin films over a wide range in conductivity, Phys. Rev. B **79**, 014431 (2009).

[39] J. Weischenberg, F. Freimuth, S. Blügel, and Y. Mokrousov, Scattering-independent anomalous Nernst effect in ferromagnets, Phys. Rev. B **87**, 060406(R) (2013).

[40] B. Zimmermann, K. Chadova, D. Ködderitzsch, S. Blügel, H. Ebert, D. V. Fedorov, N. H. Long, P. Mavropoulos, I. Mertig, Y. Mokrousov, and M. Gradhand, Skew scattering in dilute ferromagnetic alloys, Phys. Rev. B **90**, 220403(R) (2014).